Gold/silver bimetallic nanoclusters stabilized by immunoprotein: Tuning the selectivity for identification of kynurenine pathway metabolites

Ditta Ungor [a,*], Árpád Turcsányi [a,b], Bianka Torma [a], Edit Csapó [a,b,*]

[a] MTA-SZTE Lendület "Momentum" Noble Metal Nanostructures Research Group, University of Szeged, Rerrich B. sqr. 1, H-6720 Szeged, Hungary
[b] Interdisciplinary Excellence Center, Department of Physical Chemistry and Materials Science, University of Szeged, Rerrich B. sqr. 1, H-6720 Szeged, Hungary

ARTICLE INFO

ABSTRACT

Template-assisted green chemistry protocol for production of bimetallic gold/silver nanoclusters (Au/Ag NCs) with controlled noble metal composition is presented for the first time, where the synthesis of orange-emitting (λ_{em} = 634 nm) ultrasmall NCs, which exhibit outstanding kinetic stability in physiological conditions, has been carried out by γ-globulin (γG) immunoprotein as reducing and stabilizing agent. In addition to the optimization of the fabrication protocol, detailed optical and structural characteristics are also presented. In our previous work we demonstrated the applicability of γG-stabilized NCs with pure gold content for identification of the kynurenine pathway metabolites and a paper-based quick test was also designed for *L*-kynurenine (Kyn). In present work, we confirmed that the selectivity of the pure γG-Au NCs can be systematically shifted to the detection of kynurenic acid (Kyna) by controlled silver doping (~10 %). Sensing measurements were carried out in both phosphate buffer saline (PBS) solution and artificial cerebrospinal fluid (aCSF), where the calculated detection limits are 64.0 and 80.0 μM, respectively. Both the quenching process and the thermodynamic nature of the interaction between the Kyna and γG-Au/Ag NCs were interpreted, which confirm the electron-induced charge transfer between them.

1. Introduction

Tryptophan (Trp) is one of the most vital essential amino acids, which takes part in several important biological processes in the human body. During the two major pathways, the living organism can make several neurotransmitters from it, such as serotonin, melatonin, or the kynurenine-type molecules produced by the brain tissue, which can be involved in many pathological processes in the immune and nervous systems. For the neuroprotection strategies, the most important metabolite is the kynurenic acid (Kyna), which directly originates from the *L*-kynurenine during an irreversible transamination (Fig. S1). This molecule can modulate the function of various receptors and the neurotransmitter systems in the central nervous system by complex mechanisms. It can exert both antagonistic and agonistic effects in a concentration-dependent manner [1–3]. For this reason, an abnormal decrease or increase in the Kyna level can also lead to the disturbed functioning of neurotransmitter systems [4,5]. For example, reduced Kyna levels can be observed in the prefrontal cortex in Parkinson's disease [6] or in the cerebral cortex and the cerebrospinal fluid in the case of Huntington's disease [7]. Based on the abovementioned facts,

the rapid and selective monitoring of these molecules has grown into a new, exciting area in sensor development. In contrast of the expensive and complicated instrumental techniques, the nanomaterial-based quick tests can serve as a good alternative to achieve fast and appropriate diagnosis or treatment. There is an ongoing demand to identify all metabolites of this pathway, also through the development of test kits, which was the main aim of our work.

One of the most promising materials for sensor development is the family of the fluorescent noble metal nanoclusters (NCs). These ultrasmall particles contain only a few or few-ten metal atoms in the primer crystallite, therefore the size of the cores strongly influence the optical characteristics of the NCs [8]. Namely, if the cluster core contains only 3–5 atoms – especially only Au, the characteristic emission can appear near the shorter wavelengths (dominantly in the blue region) [9]. If the number of atoms is systematically increased, the red-shifting of the emission can be observed from the green to the near-infrared region [10,11]. For the synthesis, the template-assisted green chemistry method is generally applied, where the reducing and stabilizing agents are biomolecules with large excess (*e.g.* amino acids [12–14], amino acid derivatives [15,16], proteins [17–19], nucleotides [20]).

* Corresponding authors.

E-mail addresses: ungord@chem.u-szeged.hu (D. Ungor), juhaszne@chem.u-szeged.hu (E. Csapó).

Besides the number of atoms, the chemical quality has also a great influence on the optical and biomedical characteristics of the NCs. For example, the gold (Au) NCs have been the focus of attention mainly due to their stability and biocompatibility, while silver (Ag) NCs may be of interest due to their high electrical conductivity and outstanding photoluminescence properties [21]. Further advantage of silver is its lower price than gold, therefore, several cost-effective materials can be synthesized using Ag. In the literature, a lot of examples can be found about the production of NCs from Au [22,23], Ag [21] and their bimetallic versions [24,25]. While their optical signal strongly depends on the chemical environment [26], they are great candidates for optical sensors for pH [27], temperature [28], and several small biomolecules [20,29–31]. For example, X. Han and co-workers formed an Au NCs-based chemical tongue, which was suitable to detect important proteins of Alzheimer's disease in nanomolar concentration range. For the synthesis, four different thiolated peptides were applied, and the detected peptides were distinguishable in human urine [32]. Li and Zhao published an interesting work for the detection of adenosine triphosphate (ATP) by an unlabeled fluorescent Ag NCs-based sensor system [33]. For the synthesis of the Ag NCs, two hairpin DNA and a T4 DNA ligase were applied, which showed intensive fluorescence without ATP molecule. When the detectable ATP docked to the suitable position, the two DNA hybridized, therefore the hairpin opened, and fluorescence (PL) signal decreased.

Based on the literature data, the rapid fluorometric detection of the important neurotransmitter molecules has become one of the most dynamically developing research areas. In our previous publication [34] we successfully applied the γG immunoprotein mixture to synthesize monometallic Au NCs, which showed high selectivity against the *L*-kynurenine (Kyn). To continue this work, we tested in detail the effect of the controlled incorporation of silver atoms in the subnanometer sized cluster cores on the optical and structural characteristics, as well as the potential sensor application for the kynurenine pathway molecules. By tuning the composition of the nano-sensor, it would be possible to identify all members of the metabolites, so that test kits could be developed, as mentioned earlier.

2. Materials and methods

2.1. Materials

Gamma globulins from bovine blood (γG, >99 %, agarose gel electrophoresis) was obtained from Sigma-Aldrich, USA and γ-globulins (M_r = 150,000.00) from SERVA Electrophoresis GmbH, Germany was also used. Hydrogen tetrachloroaurate (HAuCl$_4$·3H$_2$O, 99.9 % (metal basis)) was supported by Alfa Aesar, Germany. Silver nitrate (AgNO$_3$, >99.9 %) was provided from Molar Chemicals, Hungary. For the sensor measurements, the *L*-Trp (1: $C_{11}H_{12}N_2O_7$, 98 %), kynurenic acid (2: $C_{10}H_7NO_3$, Kyna, 98 %), xanthurenic acid (3: $C_{10}H_7NO_4$, 96 %), *L*-kynurenine (4: $C_{10}H_{12}N_2O_3$, 98 %), 3-hydroxy-*L*-kynurenine (5: $C_{10}H_{12}N_2O_4$, 98 %), 3-hydroxyanthranilic acid (6: HOC$_6$H$_3$(NH$_2$)CO$_2$H, 97 %), anthranilic acid (7: 2-(H$_2$N)C$_6$H$_4$CO$_2$H, 98 %), picolinic acid (8: $C_6H_5NO_2$, 99 %), quinolinic acid (9: $C_7H_5NO_4$, 99 %), nicotinamide-adenine-dinucleotide (10: $C_{21}H_{27}N_7O_{14}P_2$, 97 %) were obtained from Sigma-Aldrich, USA. Sodium hydroxide (NaOH, 99 %), hydrochloric acid (HCl, 37 %), sodium chloride (NaCl, 98 %), potassium chloride (KCl, 96 %), potassium phosphate monobasic (KH$_2$PO$_4$, 99 %), sodium hydrogen carbonate (NaHCO$_3$, 98 %), D-glucose (C$_6$H$_{12}$O$_6$, 98 %), calcium chloride (CaCl$_2$, 98 %), magnesium chloride (MgCl$_2$, 99 %) chemicals were provided from Molar Chemicals, Hungary. All the chemical reagents were analytical grade and were used without further purification. The stock solutions were freshly prepared by using Milli-Q ultrapure water (18.2 MΩ·cm at 25 °C) in every case.

2.2. Synthesis of bimetallic γG-stabilized NCs

3 mg γG was added to 5 mL ultrapure water and stirred for 30 min. To the resulting opalescent solution 318.5 μL water, 174.5 μL of 10 mM HAuCl$_4$ and 17 μL of 10 mM AgNO$_3$ solutions were added (total volume is 510 μL) and stirred for another 15 min for adequate interaction between the γG and [AuCl$_4$]$^-$/Ag$^+$ (0.40 w% metal to protein, 5.07 % Ag to total metal content). After this step 400 μL of 1 M NaOH solution was added to reach the adequate pH of reaction mixture. After few minutes of mixing, the stirring was stopped, and the sample was stored at room temperature for 24 h, protected from light exposure. Finally, the sample was dialyzed protected from light in a 64 kDa molecular weight cut-off membrane against 1 L of ultrapure water for 2 h, then the matrix was changed to fresh water and dialyzed for another two hours. The purified aqueous sample was stored in refrigerator until further use. For structural characterization the purified aqueous dispersion was freeze-dried with a Christ Alpha 1–2 LD plus device. The dried lyophilized powder was stored in freezer (−20 °C) until further use

2.3. Spectrofluorometry

The characteristic reddish orange fluorescence was recorded on a JASCO FP-8500 spectrofluorometer using 1 cm optical length. For the measurements, the bandwidth was 2.5 nm, 200 nm/s as scan speed and 1 nm as resolution were applied. Excitation wavelength was 370 nm, while the emission maxima was appointed at 637 nm during the sensor measurements. For the calculation of the absolute internal quantum yield (QY %), the incident light spectra and both indirect and direct excitation were applied on the same apparatus equipped with the ABL&E JASCO ILF-835 integrating sphere in 2 mm optical length and 3 mm aperture. The registered spectra were corrected by using ABL&E JASCO ESC-842 calibrated WI light source, thus other references were not needed. The calculations were done by the ABL&E JASCO SpectraManager 2.0 software of the instrument. The lifetime decay curves were recorded by time-correlated single photon counting (TCSPC) technique on a Horiba DeltaFlex device. The instrument was equipped with a DeltaDiode pulsed laser (λ_{laser} = 371 nm), and the samples were filled into a 1 cm quartz cuvette. The emitted light was detected at 640 nm with an 8 nm slit. The number of counts on the peak channel was 500 due to the long decay and the instrument response function (IRF) was measured by standard SiO$_2$ colloids (Horiba). The main lifetime components were calculated in the EZTime program of Horiba by the exponential fitting of decay curves and the goodness of fitting was characterized by χ^2 values.

2.4. Dynamic light scattering (DLS) and ζ-potential studies

The stability of the γG-Au/Ag NCs was studied under different pH by monitoring the change of the hydrodynamic diameter (d$_H$) and Smoluchowski model-fitted ζ-potential values as a function of pH. The measurements were carried out on a Malvern Zetasizer NanoZS ZEN 4003 apparatus equipped with a He-Ne laser (λ = 633 nm, 4 mW) at 25 ± 0.1 °C applying 0.1 M ionic strength by NaCl. All samples were consecutively measured five times.

2.5. Streaming potential studies

The change of the streaming potential values as a function of pH was measured for pure protein and for the γG-Au/Ag NCs. For this purpose, a Mütek PCD 04 particle charge titrator was applied, where the initial volume was 20 mL and the data points were registered in each 0.5 pH units. The concentration of the protein was 2.54 mg mL^{-1} in the dispersions.

2.6. X-ray photoelectron spectroscopy (XPS)

To determine the oxidation state of the metal atoms in the cluster cores, XPS measurement was applied. The spectra of the lyophilized powder were registered by a SPECS instrument equipped with a PHOI-BOS 150MCD9 hemispherical analyzer in survey scan with 40 eV. In high-resolution mode, 20 eV pass energy was used. The charge reference was the carbon 1 s peak at 284.80 eV and the Al Kα X-ray source was operated at 200 W power. The spectra were analyzed by CasaXPS software.

2.7. Scanning electron microscopy – energy dispersive X-ray spectroscopy (SEM-EDX)

To identify the metals in cluster core, SEM-EDX was utilized. The EDX spectra were recorded from freeze-dried powder samples in a Hitachi S-4700 field emission scanning electron microscope using a Röntec XFlash X-ray detector, applying 25 kV acceleration voltage and 4096 detector channels for signal counting and processing. The integration time for each measurement was 180 s, and the Fano factor was 0.10484.

2.8. Inductively coupled plasma mass spectroscopy (ICP-MS)

The exact elemental composition of the bimetallic NCs after purification was determined using ICP-MS. The system consisted of a quadrupole Agilent 7700X instrument, Agilent I-AS type autosampler, a MicroMist microflow concentric pneumatic nebulizer and a Scott-type spray chamber with Peltier-cooling. The total concentrations of the metals in the samples were investigated by dissolving the NCs in hot aqua regia for 1 h. For gold, the calibration was carried out using the Agilent Multi-Element Calibration Standard-3, and for silver the Inorganic Ventures IV-ICPMS-71A. The final values were recorded at 50–60 μg L^{-1} concentrations using three parallel measurements, obtaining an RSD value of 5–6 %.

2.9. Fourier-transformed infrared spectroscopy (FT-IR)

FT-IR spectra were recorded on a JASCO FT/IR-4700, which was equipped with an ATR PRO ONE Single-reflection accessory. Spectra were registered in the range of 500 to 4000 cm^{-1} with 1 cm^{-1} resolution and 128 interferograms. The measurements were conducted on the lyophilized protein-NCs and the lyophilized protein powders after the dissolution of the immunoprotein at the same concentrations and similar pH to the cluster dispersions.

2.10. Circular dichroism (CD)

The circular dichroism (CD) spectra were recorded on a JASCO J-1100 spectrometer between 190–300 nm with 1 cm optical length at room temperature. The percentage of the secondary structure elements was calculated by the Reed model [35] with the JASCO SpectraManager 2.0 Secondary Structure Estimation program. It is well-known that for proteins the Yang model is more suitable, but the Reed provided better fitting of the data.

2.11. High resolution electron microscopy (HRTEM)

The HRTEM images were registered on Tecnai G2 instrument using 220 kV accelerating voltage, using a heated W filament (100 μm) as electron source. The recorded photos were taken using bright field setup at 100 k magnification and were analyzed with ImageJ software based on the average diameter of ~100 NCs.

2.12. Cyclic voltammetry (CV)

To analyze the electrochemical characteristic of the bimetallic and the pure γG-Au NCs, CV measurements were carried out with a Metrohm DropSense μStat 400 Bipotentiostat/Galvanostat. In the electrochemical cell, the Metrohm-manufactured screen-printed carbon electrode (SPCE) was used, where the working and counter electrode was a carbon film, and a AgCl-covered Ag electrode served as a reference electrode. The measurements were performed in 0.1 M KCl aqueous solution which contains the NCs suspension applying 50 mV/s sweep rate at 25 °C. The potential window was between −0.4 V and +1.0 V.

2.13. Detection procedures of the tryptophan metabolites

For sensor experiments, 1 mL of purified γG-Au/Ag NCs (final c_{metal} = 0.16 mM) was pipetted into separate aqueous solutions, which contained the different neuroactive molecules from the kynurenine pathway in similar concentrations (c = 0.5 mM). The final volume was 2 mL. In case of Kyna detection, the PL quenching studies were carried out in wide concentration range (from 1 nM to 4 mM). The quenching studies were carried out in phosphate buffer saline (pH = 7.4 and 0.9 % NaCl content) and in artificial cerebrospinal fluid (aCSF) solutions as biologically relevant buffer media. The composition of the aCSF solution was presented previously [34]. To understand the exact mechanism, the lifetime of the samples was determined before and after addition of 0.1 mM Kyna solution. Moreover, the quenching processes were also performed at four different temperatures (298, 303, 308 and 313 K). The PL spectra of the pure diluted γG-Au/Ag NCs solution served as reference in every case to define the relative fluorescence intensities (I_0/I).

3. Results and discussion

3.1. Optimization of the composition of γG-Au/Ag NCs

The fabrication protocol of our previously developed γG-stabilized pure Au NCs was applied with minor modifications [34]. In short, 15 mg γG was dissolved in 5.0 mL water for 2 h, then 510 μL of 10 mM HAuCl$_4$ solution was added to this solution and mixed for 15 min (1.0 mg total gold content). After proper protein–[AuCl$_4$]$^-$ interaction, 400 μL of 1 M NaOH solution was also added to adjust the sample pH to 12 to ensure the total reduction of gold ions. The sample was left without stirring for 24 h at 37 °C and it was protected from light. To create the bimetallic version, a specific quantity of gold atoms (~0–20 %) was exchanged to silver by substituting the gold stock solution to silver nitrate. The gold to silver molar ratios (AuCl$_4^-$:Ag$^+$) were investigated from 1:0 to 0:1, with special interest to the 1:0–0.80:0.20 region. Continuous increase in silver content caused the shift of the emission band from λ$_{em}$ = 675 nm to the shorter wavelength region. This blue-shift could be explained by the change of gold atoms to silver, which can change the HOMO-LUMO transition energy (from highest occupied –HOMO– to lowest unoccupied –LUMO– molecular orbital) [36]. In this case, the energy level of original LUMO (made of Au 6 s and 6p orbitals) will be altered by the introduction of Ag 5 s orbital, which is higher than the Au 6 s, thus increasing the energy gap. This variation in the metal core produces remarkable changes in the optical properties of the NCs, as shown in several articles [37] depending on the introduced element and its quantity. Finally, the AuCl$_4^-$: Ag$^+$ = 0.911:0.089 nominal molar ratio (91.1 %/8.9 %) was selected (Fig. 1A), because the largest wavelength shift (Δλ = 38 nm) of the emission band compared to the pure Au NCs was achieved to the orange region (λ$_{em}$ = 637 nm) at this composition.

Higher silver content (>10 %) caused the distortion of the emission band and the formed NCs showed lower stability and AgCl precipitation is also appeared in the sample. Next, the role of the protein concentration was also investigated, and the amount of γG was changed from the initial 15 mg in the range of 1 mg to 150 mg. At lower protein content (γG:metal mass ratio < 10:1) only colloidal nanoparticles (NPs) formed
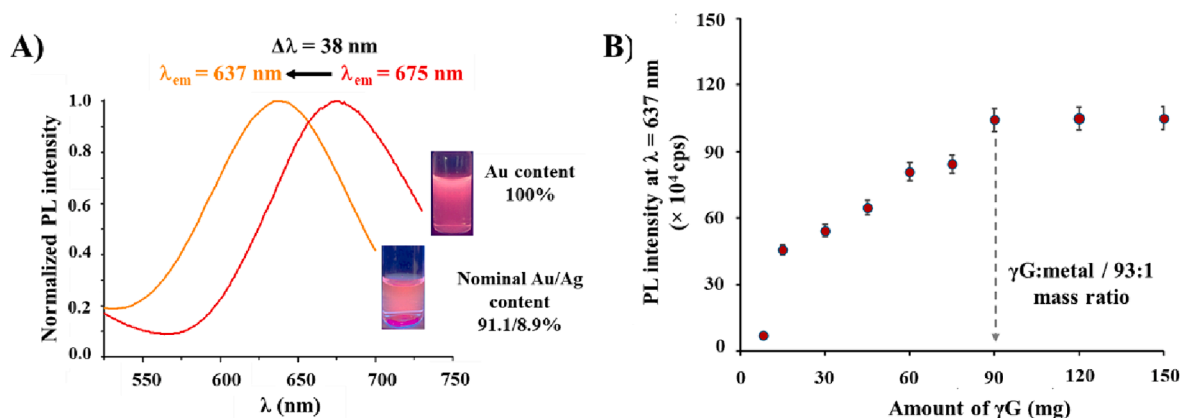
Fig. 1. (A) Normalized PL spectra of the original γG-Au NCs and the bimetallic γG-Au/Ag NCs with the photos of the samples under UV-lamp ($\lambda_{lamp} = 365$ nm), (B) PL intensities of the γG-Au/Ag NCs-containing dispersion as a function of the amount of γG (for 0.96 mg total metal content, T = 25 °C, $\lambda_{ex} = 365$ nm).

in the samples, signaled by the characteristic dark red wine color, then at higher values the color changed to pale yellow (γG:metal mass ratio >10:1), verifying the formation of NCs instead of plasmonic NPs. At sufficient γG amount (γG:metal mass ratio = 90:1–150:1), the samples showed similar PL intensities, therefore the lowest value (90 mg γG, γG: metal mass ratio = 93:1) was chosen for further experiments (Fig. 1B). Studying the effect of the synthesis temperature (in the range of 10 °C–80 °C) on the NCs' yield, we found that at 80 °C the sample turned dark brown with significant amount of flaky precipitate, showing no PL at all. At 60 °C the color is lighter with less precipitate, producing low PL intensity in the red region. When the temperature was kept at 25 °C the

color of the sample is paler compared to 37 °C, and the PL intensity is higher and shifted to lower wavelength (orange-red color is visible). At 10 °C the color is similar, but the fluorescence is much weaker after 24 h, so for future experiments the 25 °C was selected with 24 h reaction time. In examining the effect of the starting total metal content in the range of 0.3 to 3 mg we found that the samples with lower metal content showed much higher internal PL intensity compared to higher metal concentration, but this change was also followed by a red shift of the emission. The highest PL intensity was reached at 0.375 mg total metal content, which was chosen for the next procedure. In the final optimization step the reduction time was checked by continuous measurement of the PL
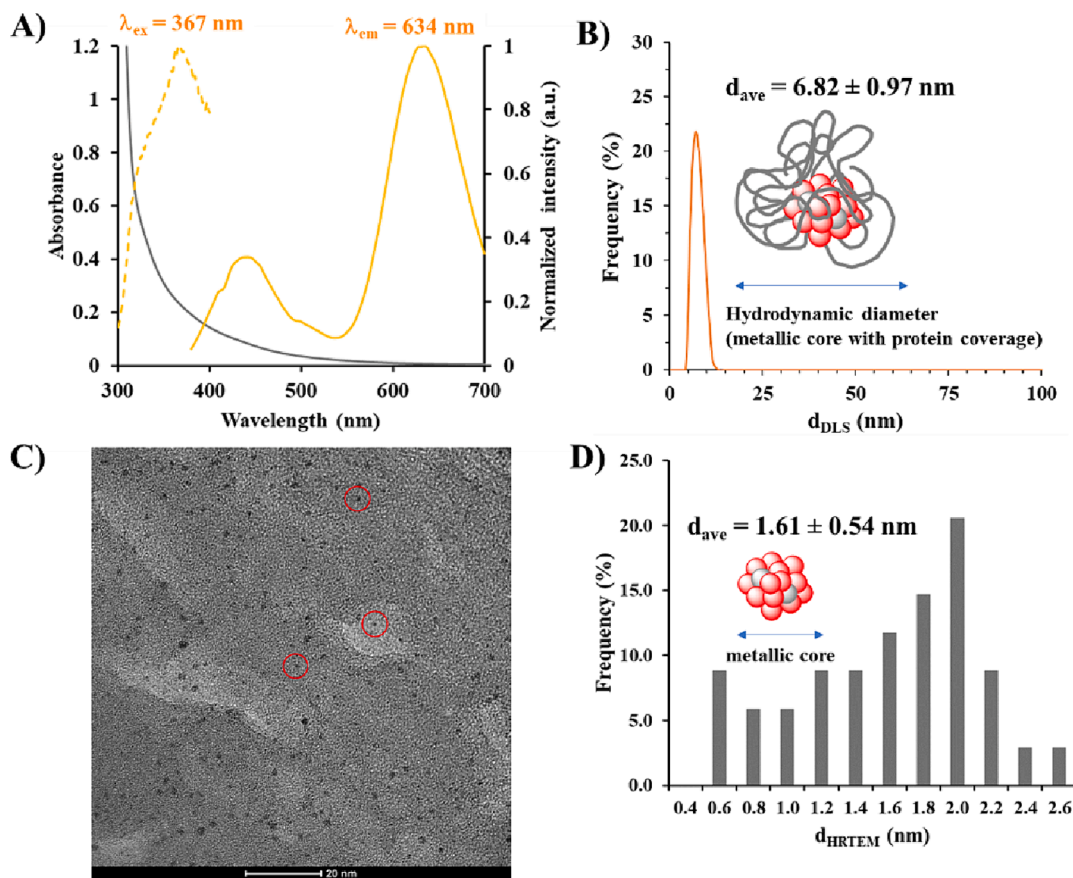

Fig. 2. (A) The absorbance (left), excitation (dashed) and normalized emission (right) spectra of γG-Au/Ag NCs (0.96 mg total metal content, T = 25 °C); (B) DLS curve of the NCs-containing aqueous dispersion at pH = 9.0; (C) Representative HRTEM image of γG-Au/Ag NCs with (D) the size distribution diagram demonstrating the average size of the metallic core at pH = 9.0.

intensity throughout the investigated timeframe. In the first few minutes after the addition of NaOH solution, the opalescent sample becomes clear, with a very pale yellow color which becomes slightly darker over time. The maximum PL intensity was detected after 24 h. After 24 h incubation time the aqueous sample was purified as mentioned in the Experimental Section for optical and structural characterization.

3.2. Characterization of the newly synthesized bimetallic Au/Ag NCs stabilized by γG

Comprehensive optical and structural characterization of the purified dispersion were performed. As Fig. 2A represents, the excitation and emission maxima of the purified immunoprotein-stabilized Au/Ag NCs can be identified at 367 and 634 nm, respectively. The observable other peak on emission spectrum at ~450 nm belongs to the original protein shoulder peak with minimal red shift, where the shift is caused by the presence of NC cores in the protein matrix. The Fig. 2A presents the UV–visible light absorption (UV–Vis) spectrum of the NCs as well. Based on the light utilization measurements, the QY (%) is 2.31 ± 0.29, while for TCSPC experiments three different lifetime components were identified, which are $\tau_1 = 99.7 \pm 37.5$ ns (4.72 %), $\tau_2 = 1.259 \pm 0.071$ μs (93.46 %) and $\tau_3 = 2.7 \pm 0.5$ μs (1.82 %). Based on the literature data [38], it is well-known that the nanosecond-ranged τ_1 refers to the metal–metal charge transfer between the Au and Ag atoms in the cluster cores, while the μs-ranged τ_2 and τ_3 belong to ligand-dependent charge transfers in the case of protein-stabilized metal NCs. Based on DLS measurements (Fig. 2B), the hydrodynamic diameter of NCs (covered by immunoprotein) could be determined as $d_H = 6.82$ nm ± 0.97 nm, which is quite similar to the monometallic NCs, as reported previously [34]. The metal cores are much smaller in size, which is confirmed by HRTEM images (d = 1.61 nm ± 0.54 nm) (Fig. 2C,D). On HRTEM images only the metallic core can be identified, the presence of protein shell cannot be detected based on the applied high accelerating voltage.

Streaming potential measurements were performed to confirm the presence of a metallic core in the protein matrix. Fig. 3B shows that the isoelectric point (i.e. p) of the γG protein (i.e. p = 4.6–6.5) [39] was shifted by a whole pH unit towards the acidic range thanks to the absence of the charged functional groups that play a role in cluster core binding. Analyzing the stability of the NCs via measuring the change of cluster size and PL intensity as a function of pH (Fig. 3B) we can state that, in agreement with the results of Fig. 3A, in the vicinity of the i.e.p both the average size and PL intensity show increased values. For PL intensity a larger increase in values can be observed thanks to the aggregation induced emission enhancement (Fig. 3B), even though the synthesized Au/Ag NCs do not show remarkable aggregation; the hydrodynamic diameter increases from ~7 nm to ~20 nm. The salt tolerance of the dispersion was also studied over a wide salt

concentration range ($c_{NaCl} = 0$–2.5 M) and as Fig. S2 presents, the increase in the salt concentration does not influence the characteristic PL intensity of the NCs. The stability of the samples during storage differs based on several factors. Light exposure causes fast decrease of the fluorescence, so the samples should always be protected from light. Protected from moisture, lyophilized powders can be stored for months at −20 °C without huge loss of fluorescence but storing at room temperature is also feasible for at least a week. Storage in dissolved form should be as short as possible (one week at 4 °C) due to the decrease of emission value over time. For longer storage, the sample should be stored before dialysis to better preserve its optical properties. The protein in the samples is also sensitive to storage, after enough time degradation and slight aggregation occurs, the formation of aggregates becomes visible after 24 h at room temperature or after one week at 4 °C.

For the investigation of the metal content in the NCs, the XPS spectra were recorded. As Fig. 4A represents, only the Au can be identified from the metal content due to the large protein excess and small Ag amount in the cluster cores. Based on the high-resolution mode (Fig. 4B), the Au is in Au^0 oxidation state because the Au $4f_{7/2}$ and $4f_{5/2}$ are at 84.05 eV and 87.80 eV, respectively, which are in good agreement with the corresponding values of metallic gold [40]. The XPS results were supported by SEM-EDX measurements of dried samples presented in Fig. S3. Similarly, only the presence of Au could be detected by this method, which further proves the presence of metal in the dialyzed sample.

To accurately determine the metal content of the final sample, ICP-MS was utilized. Based on the results presented in Table 1, we could see that after reduction of the metal ions and the purification step the nominal gold content decreased while Ag remained similar to the theoretical value. The actual Au:Ag ratio thus shifted from 91.1:8.9 to 89.2:10.8 in the final sample. It can be concluded that the procedure developed to produce these bimetallic NCs shows high efficiency and reproducibility.

For structural analysis of the formed bimetallic NCs, FT-IR and CD studies have also been carried out. The amide I peaks belonging to the different secondary structure elements of the protein [41] (β-sheets: two peaks at 1691–1680 and 1642–1621 cm^{-1}, α-helix 1657–1653 cm^{-1}, coils and β-turn: 1677–1661 cm^{-1}, random: 1657–1642 cm^{-1}) are shown in Fig. S4A. Due to the cluster formation, the contribution of β-sheets goes down, while the amount of random coil structure increases, showing the disorganization of the initial protein structure (Fig. S4B). The other secondary elements show little to no changes according to our measurements, with α-helices having no remarkable contribution in accordance with the literature. The results of CD studies show similar changes in the protein structure as IR measurements.

As shown in Table 2, the contributions of β-sheets, random coils and β-turns are deciding, and the α-helix content is almost negligible, which is also visible on the deconvoluted IR spectra (see Fig. S4). The
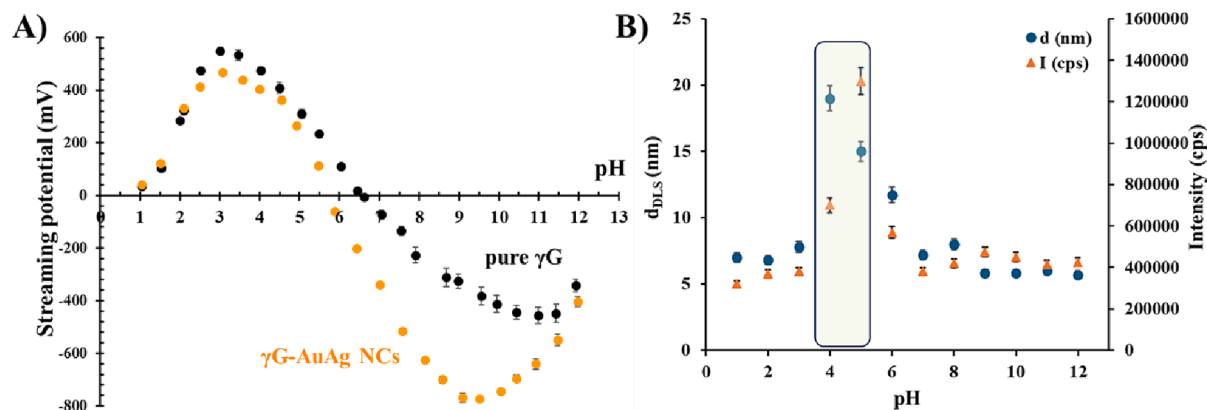

Fig. 3. (A) Streaming potentials for pure γG and γG-Au/Ag as a function of pH ($c_{\gamma G} = 2.54$ mg cm^{-3}, T = 25 °C); (B) The hydrodynamic diameters (●) and the emission intensities (▲) of the diluted NCs suspension (total metal content is 0.5 mg) depending on the pH ($\lambda_{ex} = 367$ nm).
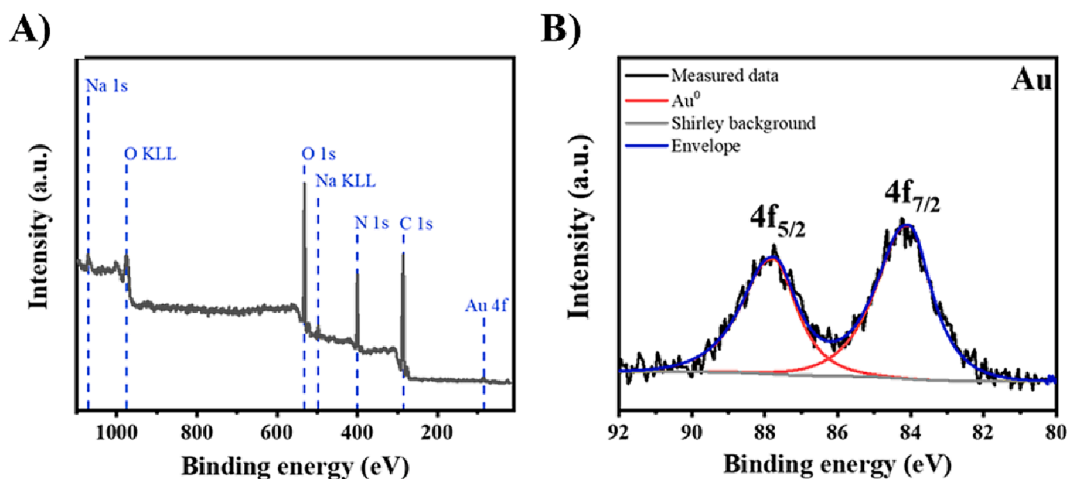
Fig. 4. XPS spectra in (A) survey scan and (B) the Au content of the γG-Au/Ag NCs in high-resolution mode.

Table 1
Element composition of γG-Au/Ag NCs according to the calculated values and the actual concentrations measured by ICP-MS.

Metal	Nominal value (mg mL^{-1})	Nominal molar ratio (%)	Actual value (mg mL^{-1})*	Actual molar ratio (%)
Au	0.0582	91.1	0.0435	89.2
Ag	0.00310	8.9	0.00290	10.8

* RSD = 5–6 %.

Table 2
Contribution of secondary structural elements to the CD spectra of γG and γG-Au/Ag NCs according to the Reed model [35].

	α-helix	β-sheet	coils, β-turn	random
γG	0	40.0	20.8	39.2
γG-Au/Ag NCs	0	36.0	13.1	50.9

formation of NCs decreases the values belonging to coils, β-turns, while the contribution of random coils has a large increase, further proving the disorganizing effect of the newly formed metal cores.

Besides the stability and structural studies, the electrochemical characteristic of the Au/Ag NCs was also examined (Fig. S5), where only one oxidation peak was identified at 0.551 V (vs Ag/AgCl in 0.1 M KCl). This peak clearly refers to the real alloying seeds, as the Au NCs show two peaks at 0.562 and 0.725 V (vs Ag/AgCl in 0.1 M KCl) [42]. Besides, the Au/Ag NCs show much higher electroactivity due to the presence of silver atoms in cluster cores. Therefore, the transfer of the energy excess is preferable during a simple fluorescence-based sensing process [43,44].

3.3. Interaction with the kynurenine pathway molecules

To utilize the NCs as potential turn-off sensors for the kynurenine pathway molecules, the direct interaction with ten determining molecules were tested. For this purpose, 0.5 mM solutions of these molecules were mixed with the cluster dispersion and the relative fluorescence values (I_0/I) were calculated to analyze the selectivity (Fig. 5A). The studies were carried out in PBS and in aCSF media as well. Based on the registered data, it can be stated that the Au/Ag bimetallic NCs is sensitive to the presence of Kyna ($I_0/I \sim 9$) and 3-hydroxy-*L*-kynurenine ($I_0/I \sim 5$) in PBS. Higher quenching, thus more selective identification for Kyna can be achieved in aCSF medium ($I_0/I \sim 16$) compared to the pure Au clusters ($I_0/I \sim 1$) [34]. For determination of the smallest detectable amount (LOD) in both buffers, the standardized method of H. P. Loock and P. D. Wentzell [45] was applied, which resulted *ca.* 64 and 80 μM in
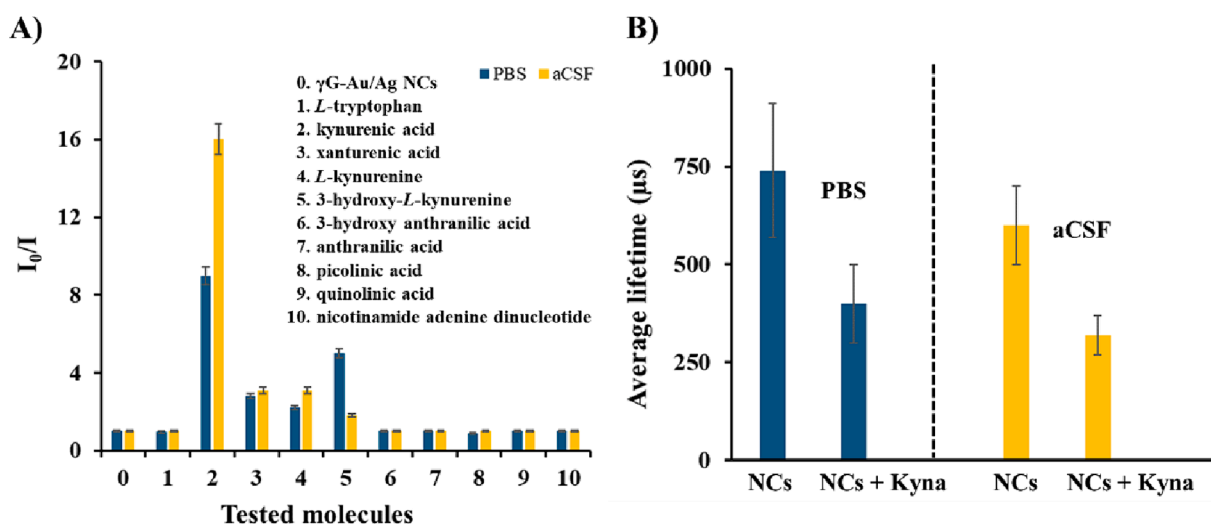

Fig. 5. (A) The relative fluorescence intensities (I_0/I) before and after addition of 0.5 mM kynurenine pathway molecules in PBS and in aCSF. (B) The average fluorescence lifetime of the γG-Au/Ag NCs before and after addition of 100 μM Kyna in PBS (left) and aCSF (right).

PBS and aCSF, respectively. To better understand the exact detection mechanism, two different methods were applied. First, the TCSPC measurements were selected for the investigation of the average fluorescence lifetime of Au/Ag NCs before and after addition of Kyna. Fig. S6 presents the characteristic decay curves of the NCs before and after addition of Kyna, while Fig. 5B shows the determined average lifetime values. The average lifetime drastically decreased by *ca.* 45 % after the addition of Kyna. Namely, the measured τ changed from 0.75 µs to 0.42 µs in PBS, while in aCSF medium the 0.61 µs changed to 0.33 µs.

This clearly refers to the presence of dynamic quenching rather than static, which means energy loss by collision. Next, the temperature-dependent measurements were carried out to prove the exclusive presence of dynamic quenching. For this purpose, the quenching process was executed at four different temperatures (25, 30, 35 and 40 °C). For the evaluation of the registered data, the Stern-Volmer equation was applied [46]:$I_0/I = 1 + K_{SV}[Q]$ (1) where I_0 and I are the maximum of the fluorescence intensity before and after addition of Kyna, the K_{SV} is the Stern-Volmer quenching constant and the $[Q]$ is the equilibrium concentration of Kyna (without any further independent measurements, the analytical concentration can be generally used). Fig. 6 demonstrates the Stern-Volmer representation of the data in PBS (Fig. 6A) and in aCSF (Fig. 6C). At lower temperatures (298 and 303 K) a linear can be fitted to the measurement points, which is the result of pure dynamic quenching, but at higher temperature values (308, 313 K) the observed positive deviation in the Stern-Volmer plots at high concentrations of Kyna, as shown in Fig. 6A and C, suggests that a combination of dynamic and static mechanisms may be at play, rather than a pure dynamic mechanism. This finding aligns with previous research [47]. The determined K_{SV}, which is the slope of the line fitted to the points on Fig. 6A and C, increased with the temperature (Table 3) referring the dynamic quenching.

Based on temperature-dependence PL quenching studies the combined (dynamic + static) quenching cannot be excluded, and we can presume that the quenching works through the nonradiative

Table 3
The applied temperature (T), the determined Stern-Volmer constants (K_{SV}) and the values of the estimated thermodynamic parameters ($\Delta H°$, $\Delta S°$, $\Delta C_p°$) in PBS and aCSF media.

	T (K)	K_{SV} (M^{-1})	ΔH^0 (kJ mol^{-1})	$\Delta S°$ (kJ mol^{-1} K^{-1})	$\Delta C_p°$ (kJ mol^{-1} K^{-1})
PBS	298	2266 ± 291	71.47 ± 2.40	0.30 ± 0.01	3.12 ± 0.28
	303	3831 ± 186			
	308	4503 ± 474			
	313	6075 ± 571			
aCSF	298	3301 ± 248	54.50 ± 2.58	0.25 ± 0.01	1.83 ± 0.42
	303	4898 ± 334			
	308	5881 ± 543			
	313	7490 ± 344			

photoinduced charge transfer (PCT) mechanism which is favored in many sensor applications [48–50]. The charge transfer can be an excitation electron-induced proton transfer between the Kyna and the protein shell [49,51]. Specifically, the Kyna molecules can donate protons to the protein shell of the NCs, and the modified corona can alter the electronic energy distribution in the cluster metal cores, and open a new channel for nonradiative relaxation. The addition of Kyna suppressed the fluorescence of the NCs without changing the shape of the emission curve and also decreased the fluorescence lifetime, which further proves the PCT [48]. The possibility of Förster resonance energy transfer (FRET) in the Kyna-NCs system can be excluded due to the lack of a noticeable overlap between the absorption band of Kyna and the
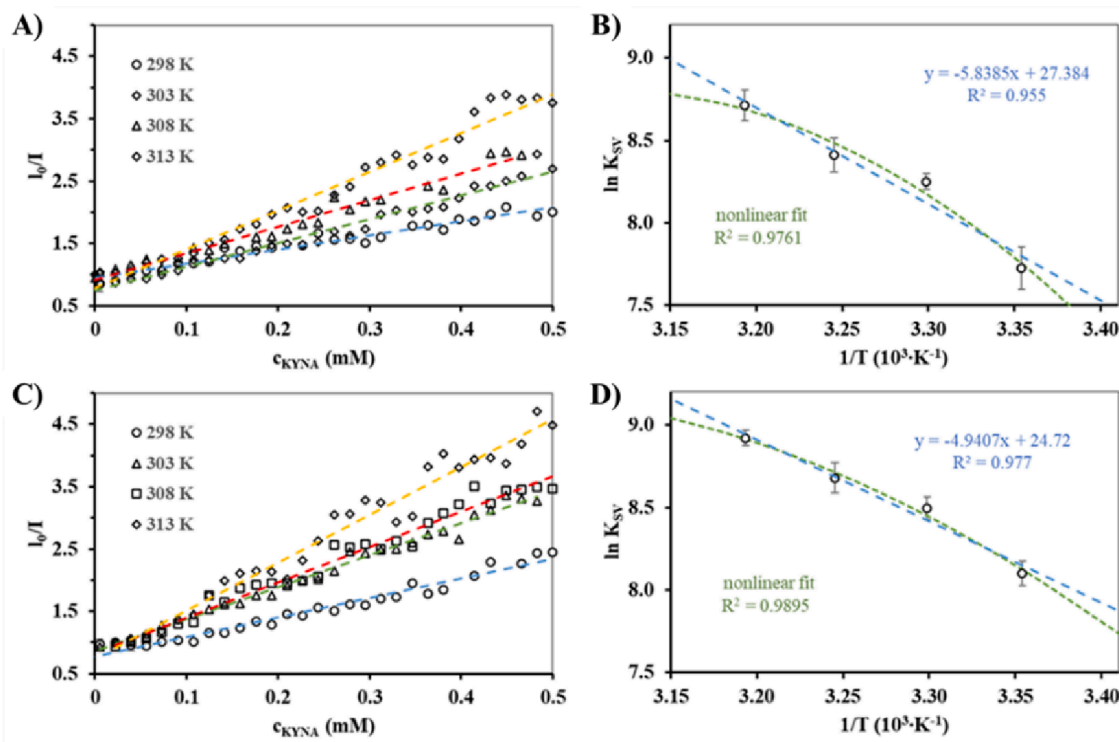

Fig. 6. Stern-Volmer representation (I_0/I vs. c_{Kyna}) in PBS and in aCSF (A) and (C). Linear (larger blue dashed lines) and non-linear (smaller green dashed curves) van't Hoff evaluation of the temperature dependence of the quenching constant in PBS and aCSF (B) and (D).

emission band of Au/Ag NCs [49]. In our case, a bimolecular collision takes place between the Au/Ag NCs and the Kyna via a transient complex formation. The selectivity of our NCs can be explained through the stability of this complex. By the applied conditions (pH = 7.4) –OH group present on the aromatic ring can be responsible for the donation of the proton, as carboxylic groups are fully deprotonated at this pH. Furthermore, the investigated molecules show a measurable quenching effect only when they possess –OH, –NH$_2$ or ketone groups directly linked to the aromatic rings, which can participate in the stabilization of the surplus negative charge through mesomerism (keto enole tauromerism). In the end, the reaction leads to the energy transfer between the partners and the disintegration of the transient complex. The hypothetic reaction scheme is the following (Eq. (2)):

$$Au/Ag\ NCs^* + Kyna \rightleftharpoons [Au/Ag\ NCs - Kyna]^{\ddagger} \rightarrow Au/Ag\ NCs + Kyna^* \quad (2)$$
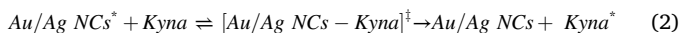
where the * represents the excitation state of the components.

Based on this assumption the $\mathbf{K_{SV}}$ can be treated as the formation constant of the transient complex, therefore the thermodynamic nature can also be determined by the non-linear van't Hoff evaluation (Fig. 6B and D). The thermodynamic parameters were calculated by Eq. (3) [52] and the data are summarized in Table 3:

$$\ln K_{SV} = -\Delta H^0(T^0)/RT + \Delta S^0(T^0)/R + \Delta C_p/R \left[\left((T - T^0)/T \right) - \ln \left(T/T^0 \right) \right] \quad (3)$$

where $\mathbf{T}$ is the absolute temperature, $\mathbf{T^\circ}$ is an arbitrary temperature, $\mathbf{\Delta H^\circ}$ is the standard enthalpy change, $\mathbf{\Delta S^\circ}$ is the standard entropy change, while the $\mathbf{\Delta C_p}$ is the heat capacity.

As it can be seen from the determined data, the quenching process by Kyna is thermodynamically favored because the calculated $\mathbf{\Delta G}$ are negative at all investigated temperature values ($\mathbf{\Delta G}$ = -19 kJ mol^{-1} (298 K)). As the entropy member $|\mathbf{T\Delta S^\circ}|$ is higher than the absolute value of $\mathbf{\Delta H^\circ}$, entropy-driven quenching can be assumed as in the case of Au NCs, which is also supported by the suggested mesomerism of the transition complex. The positive value of the $\mathbf{\Delta H^\circ}$ refers to the endothermic reaction via charge transfer [53]. By comparing the quenching mechanism of these bimetallic NCs with the corresponding result of pure Au NCs [34], it was found that the same processes can be identified, but by incorporating silver into the cluster core, a new electron structure is formed that can tune the selectivity of the previously developed nanostructured sensor.

4. Conclusion

In this article a simple "green" preparation protocol was developed for synthesis of highly fluorescent bimetallic Au/Ag NCs with the use of γ-globulin immunoprotein as protein template. The prepared NCs have ~90:10 gold to silver molar ratio, and an orange-red emission with maximum value at 634 nm (λ_{ex} = 367 nm). The fluorescence quantum yield (*ca.* 2.3 %) cannot change drastically compared to pure γ-globulin-stabilized Au clusters (*ca.* 2.2 %), and the fluorescence lifetime measurements pointed out the complex fluorescence mechanism based on the calculated three lifetime components. We determined that the presence of the metallic seeds in the protein matrix can decrease the isoelectric point of the γG with ~1 pH unit, while the FT-IR and CD studies strongly imply the disorganization of the initial protein structure after cluster formation. The prepared Au/Ag NCs show high stability under physiological conditions. Storage before further application should always be conducted using light protection and not longer than one week at 4 °C due to the decrease of emission value and protein degradation over time. The lyophilized powder form can be stored for months at −20 °C without huge loss of fluorescence. During the possible sensor applications, ten of the kynurenine pathway molecules were

tested, where the Kyna caused the most intensive decrease in the fluorescence intensity in PBS and aCSF biological medium. The LOD values are 64 and 80 μM in PBS and aCSF, respectively, while the lifetime measurements refer to the dominant dynamic or combined quenching process between the Au/Ag NCs and Kyna, indicating photoinduced charge transfer mechanism. Besides, the temperature-dependent measurements clearly show that the quenching process is entropy-driven and endothermic via electron-induced proton transfer.

CRediT authorship contribution statement

Ditta Ungor: Writing – original draft, Methodology, Investigation, Conceptualization. **Árpád Turcsányi:** Writing – original draft, Methodology, Investigation. **Bianka Torma:** Methodology, Investigation. **Edit Csapó:** Writing – review & editing, Writing – original draft, Visualization, Supervision, Project administration, Conceptualization.

Declaration of competing interest

The authors declare that they have no known competing financial interests or personal relationships that could have appeared to influence the work reported in this paper.

Data availability

Data will be made available on request.

Appendix A. Supplementary data

Supplementary data to this article can be found online at https://doi.org/10.1016/j.molliq.2024.124756.

References

[1] C. Prescott, A.M. Weeks, K.J. Staley, K.M. Partin, Kynurenic acid has a dual action on AMPA receptor responses, Neurosci. Lett. 402 (2006) 108–112, https://doi.org/10.1016/J.NEULET.2006.03.051.

[2] R. Carpenedo, A. Pittaluga, A. Cozzi, S. Attucci, A. Galli, M. Raiteri, F. Moroni, Presynaptic kynurenate-sensitive receptors inhibit glutamate release, Eur. J. Neurosci. 13 (2001) 2141–2147, https://doi.org/10.1046/J.0953-816X.2001.01592.X.

[3] H.Q. Wu, A. Rassoulpour, R. Schwarcz, Kynurenic acid leads, dopamine follows: A new case of volume transmission in the brain? J. Neural Transm. 114 (2007) 33–41, https://doi.org/10.1007/S00702-006-0562-Y/METRICS.

[4] A.B. Dounay, J.B. Tuttle, P.R. Verhoest, Challenges and opportunities in the discovery of new therapeutics targeting the kynurenine pathway, J. Med. Chem. 58 (2015) 8762–8782, https://doi.org/10.1021/ACS.JMEDCHEM.5B00461/ASSET/IMAGES/MEDIUM/JM-2015-00461H_0024.GIF.

[5] D.C. Maddison, F. Giorgini, The kynurenine pathway and neurodegenerative disease, Semin. Cell Dev. Biol. 40 (2015) 134–141, https://doi.org/10.1016/J.SEMCDB.2015.03.002.

[6] D. Venkatesan, M. Iyer, A. Narayanasamy, K. Siva, B. Vellingiri, Kynurenine pathway in Parkinson's disease—An update, ENeurologicalSci. 21 (2020) 100270, https://doi.org/10.1016/j.ensci.2020.100270.

[7] M. Flint Beal, W.R. Matson, E. Storey, P. Milbury, E.A. Ryan, T. Ogawa, E.D. Bird, Kynurenic acid concentrations are reduced in Huntington's disease cerebral cortex, J. Neurol. Sci. 108 (1992) 80–87, https://doi.org/10.1016/0022-510X(92)90191-M.

[8] Y. Li, M. Zhou, R. Jin, Programmable metal nanoclusters with atomic precision, Adv. Mater. 33 (2021) 2006591, https://doi.org/10.1002/ADMA.202006591.

[9] D. Bain, S. Maity, T. Debnath, A.K. Das, A. Patra, Luminescent Au6 and Au8 nanoclusters from ligand induced etching of Au nanoparticles, Mater. Res. Express. 6 (2019) 124004, https://doi.org/10.1088/2053-1591/ab5c8b.

[10] Y. Xu, J. Sherwood, Y. Qin, D. Crowley, M. Bonizzoni, Y. Bao, The role of protein characteristics in the formation and fluorescence of Au nanoclusters, Nanoscale. 6 (2014) 1515–1524, https://doi.org/10.1039/c3nr06040c.

[11] A. Soleilhac, F. Bertorelle, C. Comby-Zerbino, F. Chirot, N. Calin, P. Dugourd, R. Antoine, Size characterization of glutathione-protected gold nanoclusters in the solid, liquid and gas phases, J. Phys. Chem. c. 121 (2017) 27733–27740, https://doi.org/10.1021/acs.jpcc.7b09500.

[12] E. Csapó, D. Ungor, Z. Kele, P. Baranyai, A. Deák, Á. Juhász, L. Janovák, I. Dékány, Influence of pH and aurate/amino acid ratios on the tuneable optical features of gold nanoparticles and nanoclusters, Colloids Surfaces A Physicochem. Eng. Asp. 532 (2017) 601–608, https://doi.org/10.1016/J.COLSURFA.2017.02.047.

[13] E. Csapó, D. Ungor, Á. Juhász, G.K. Tóth, I. Dékány, Gold nanohybrid systems with tunable fluorescent feature: Interaction of cysteine and cysteine-containing peptides with gold in two- and three-dimensional systems, Colloids Surfaces A Physicochem. Eng. Asp. 511 (2016) 264–271, https://doi.org/10.1016/J.COLSURFA.2016.10.003.

[14] R. Bélteki, L. Kuklis, G. Gombár, D. Ungor, E. Csapó, The role of the amino acid molecular characteristics on the formation of fluorescent gold- and silver-based nanoclusters, Chem. – A Eur. J. 29 (2023) e202300720.

[15] G. Gombár, D. Ungor, I. Szatmári, Á. Juhász, E. Csapó, Tryptophanhydroxamic acid-stabilized ultrasmall gold nanoclusters: Tuning the selectivity for metal ion sensing, Nanomater. 14 (2024) 434, https://doi.org/10.3390/NANO14050434.

[16] G. Gombár, P. Simon, D. Ungor, I. Szatmári, E. Csapó, Histidinehydroxamic acid as new biomolecule to produce molecular-like fluorescent gold nanoclusters: Possible mechanisms for metal ion sensing, J. Mol. Liq. 387 (2023) 122597, https://doi.org/10.1016/j.molliq.2023.122597.

[17] M.K. Barman, B. Paramanik, D. Bain, A. Patra, Light harvesting and white-light generation in a composite of carbon dots and dye-encapsulated BSA-protein-capped gold nanoclusters, Chem. – A Eur. J. 22 (2016) 11699–11705, https://doi.org/10.1002/CHEM.201601849.

[18] Q.Q. Zhuang, S. Bin He, K.Y. Huang, H.P. Peng, C.M. Chen, H.H. Deng, X.H. Xia, W. Chen, G.L. Hong, Decisive role of pH in synthesis of high purity fluorescent BSA-Au20 nanoclusters, Spectrochim. Acta Part A Mol. Biomol. Spectrosc. 239 (2020) 118520, https://doi.org/10.1016/J.SAA.2020.118520.

[19] J.M. Dixon, S. Egusa, Common motif at the red luminophore in bovine serum albumin-, ovalbumin-, trypsin-, and insulin-gold complexes, J. Phys. Chem. Lett. 12 (2021) 2865–2870, https://doi.org/10.1021/ACS.JPCLETT.1C00222/SUPPL_FILE/JZ1C00222_SI_001.PDF.

[20] D. Ungor, I. Szilágyi, E. Csapó, Yellow-emitting Au/Ag bimetallic nanoclusters with high photostability for detection of folic acid, J. Mol. Liq. 338 (2021) 116695, https://doi.org/10.1016/j.molliq.2021.116695.

[21] Z. Han, X.Y. Dong, P. Luo, S. Li, Z.Y. Wang, S.Q. Zang, T.C.W. Mak, Ultrastable atomically precise chiral silver clusters with more than 95% quantum efficiency, Sci. Adv. 6 (2020) 107–114, https://doi.org/10.1126/sciadv.aay0107.

[22] M. Zhou, C. Zeng, Q. Li, T. Higaki, R. Jin, Gold Nanoclusters: Bridging Gold Complexes and Plasmonic Nanoparticles in Photophysical Properties, Nanomater. 2019, Vol. 9, Page 933. 9 (2019) 933. 10.3390/NANO9070933.

[23] Nonappa, Luminescent gold nanoclusters for bioimaging applications, Beilstein J. Nanotechnol. 1142. 11 (2020) 533–546. 10.3762/BJNANO.11.42.

[24] D. Bain, S. Maity, A. Patra, Surface motifs regulated aggregation induced emission in gold-silver nanoclusters, Chem. Commun. 56 (2020) 9292–9295, https://doi.org/10.1039/d0cc03565c.

[25] R. Juarez-Mosqueda, S. Malola, H. Häkkinen, Stability, electronic structure, and optical properties of protected gold-doped silver Ag29-xAux (x = 0–5) nanoclusters, Phys. Chem. Chem. Phys. 19 (2017) 13868–13874, https://doi.org/10.1039/c7cp01440f.

[26] B. Peng, J.F. Zhou, M. Ding, B.Q. Shan, T. Chen, K. Zhang, Structural water molecules dominated p band intermediate states as a unified model for the origin on the photoluminescence emission of noble metal nanoclusters: from monolayer protected clusters to cage confined nanoclusters, Sci. Technol. Adv. Mater. 24 (2023), https://doi.org/10.1080/14686996.2023.2210723.

[27] R. Ali, S.M. Saleh, S.M. Aly, Fluorescent gold nanoclusters as pH sensors for the pH 5 to 9 range and for imaging of blood cell pH values, Microchim. Acta. 184 (2017) 3309–3315, https://doi.org/10.1007/s00604-017-2352-7.

[28] W. Zhou, J. Zhu, Y. Teng, B. Du, X. Han, S. Dong, Novel dual fluorescence temperature-sensitive chameleon DNA-templated silver nanocluster pair for intracellular thermometry, Nano Res. 11 (2018) 2012–2023, https://doi.org/10.1007/s12274-017-1817-7.

[29] D. Yang, M. Luo, J. Di, Y. Tu, J. Yan, Gold nanocluster-based ratiometric fluorescent probes for hydrogen peroxide and enzymatic sensing of uric acid, Microchim. Acta. 185 (2018) 1–7, https://doi.org/10.1007/S00604-018-2823-5/TABLES/3.

[30] S. Ma, J. Wang, G. Yang, J. Yang, D. Ding, M. Zhang, Copper(II) ions enhance the peroxidase-like activity and stability of keratin-capped gold nanoclusters for the colorimetric detection of glucose, Microchim. Acta. 186 (2019) 1–7, https://doi.org/10.1007/S00604-019-3395-8/FIGURES/5.

[31] Z. Li, T. Zhang, M. Zhang, W. Hu, Detection of folic acid and imaging of folate receptor overexpressed cancer cells via a far-red silver nanoclusters with Baseline Resolved Between Excitation and Emission, Dye. Pigment. 198 (2022) 109984, https://doi.org/10.1016/J.DYEPIG.2021.109984.

[32] X. Han, Z. Man, S. Xu, L. Cong, Y. Wang, X. Wang, Y. Du, Q. Zhang, S. Tang, Z. Liu, W. Li, A gold nanocluster chemical tongue sensor array for Alzheimer's disease diagnosis, Colloids Surfaces B Biointerfaces. 173 (2019) 478–485, https://doi.org/10.1016/j.colsurfb.2018.10.020.

[33] X. Li, H. Zhang, Y. Zhao, L. Lian, X. Wang, W. Gao, B. Zhu, D. Lou, Design and synthesis of Ag nanocluster molecular beacon for adenosine triphosphate detection, J. Anal. Methods Chem. 2019 (2019), https://doi.org/10.1155/2019/2786156.

[34] D. Ungor, K. Horváth, I. Dékány, E. Csapó, Red-emitting gold nanoclusters for rapid fluorescence sensing of tryptophan metabolites, Sensors Actuators, B Chem. 288 (2019) 728–733, https://doi.org/10.1016/j.snb.2019.03.026.

[35] J. Reed, T.A. Reed, A set of constructed type spectra for the practical estimation of peptide secondary structure from circular dichroism, Anal. Biochem. 254 (1997) 36–40, https://doi.org/10.1006/abio.1997.2355.

[36] S. Wang, X. Meng, A. Das, T. Li, Y. Song, T. Cao, X. Zhu, M. Zhu, R. Jin, A 200-fold quantum yield boost in the photoluminescence of silver-doped AgxAu25-x nanoclusters: The 13th silver atom matters, Angew. Chemie - Int. Ed. 53 (2014) 2376–2380, https://doi.org/10.1002/anie.201307480.

[37] C. Zhu, J. Xin, J. Li, H. Li, X. Kang, Y. Pei, M. Zhu, Fluorescence or phosphorescence? The metallic composition of the nanocluster kernel does matter, Angew. Chemie - Int. Ed. 61 (2022) e202205947.

[38] T.Q. Yang, B. Peng, B.Q. Shan, Y.X. Zong, J.G. Jiang, P. Wu, K. Zhang, Origin of the photoluminescence of metal nanoclusters: From metal-centered emission to ligand-centered emission, Nanomaterials. 10 (2020) 261, https://doi.org/10.3390/nano10020261.

[39] A. Elkak, T. Yehya, I. Salloub, F. Berry, A one step separation of immunoglobulin G from bovine serum by pseudobioaffinity chromatography on histidine grafted to epoxy activated sepharose, Biotechnol. Bioprocess Eng. 17 (2012) 584–590, https://doi.org/10.1007/s12257-011-0496-6.

[40] S. Peters, S. Peredkov, M. Neeb, W. Eberhardt, M. Al-Hada, Size-dependent XPS spectra of small supported Au-clusters, Surf. Sci. 608 (2013) 129–134, https://doi.org/10.1016/j.susc.2012.09.024.

[41] E. Goormaghtigh, J.M. Ruysschaert, V. Raussens, Evaluation of the information content in infrared spectra for protein secondary structure determination, Biophys. J. 90 (2006) 2946–2957, https://doi.org/10.1529/biophysj.105.072017.

[42] S. Park, D. Lee, Synthesis and electrochemical and spectroscopic characterization of biicosahedral Au 25 clusters, Langmuir. 28 (2012) 7049–7054, https://doi.org/10.1021/la300817j.

[43] D. Ghosh, M. Bodiuzzaman, A. Som, S. Raja, A. Baksi, A. Ghosh, J. Ghosh, A. Ganesh, P. Samji, S. Mahalingam, D. Karunagaran, T. Pradeep, Internalization of a preformed atomically precise silver cluster in proteins by multistep events and emergence of luminescent counterparts retaining bioactivity, J. Phys. Chem. c. 123 (2019) 29408–29417, https://doi.org/10.1021/acs.jpcc.9b07765.

[44] M.A.H. Muhammed, L.K. Cruz, A.H. Emwas, A.M. El-Zohry, B. Moosa, O. F. Mohammed, N.M. Khashab, Pillar[5]arene-Stabilized Silver Nanoclusters: Extraordinary Stability and Luminescence Enhancement Induced by Host-Guest Interactions, Angew. Chemie - Int. Ed. 58 (2019) 15665–15670, https://doi.org/10.1002/anie.201906740.

[45] H.P. Loock, P.D. Wentzell, Detection limits of chemical sensors: Applications and misapplications, Sensors Actuators, B Chem. 173 (2012) 157–163, https://doi.org/10.1016/j.snb.2012.06.071.

[46] J.R. Lakowicz, Principles of fluorescence spectroscopy, Princ. Fluoresc. Spectrosc. (2006) 1–954, https://doi.org/10.1007/978-0-387-46312-4.

[47] S.M. Aly, L.G. Abdulhalim, T.M.D. Besong, G. Soldan, O.M. Bakr, O.F. Mohammed, Ultrafast static and diffusion-controlled electron transfer at Ag29 nanocluster/molecular acceptor interfaces, Nanoscale. 8 (2016) 5412–5416, https://doi.org/10.1039/c5nr05328e.

[48] H.H. Deng, K.Y. Huang, C.T. Zhu, J.F. Shen, X.P. Zhang, H.P. Peng, X.H. Xia, W. Chen, Bell-shaped electron transfer kinetics in gold nanoclusters, J. Phys. Chem. Lett. 12 (2021) 876–883, https://doi.org/10.1021/acs.jpclett.0c03617.

[49] K.Y. Huang, L.F. Xiu, X.Y. Fang, M.R. Yang, H.A.A. Noreldeen, W. Chen, H.H. Deng, Highly efficient luminescence from charge-transfer gold nanoclusters enabled by lewis acid, J. Phys. Chem. Lett. 13 (2022) 9526–9533, https://doi.org/10.1021/acs.jpclett.2c02724.

[50] K.Y. Huang, X. Huang, X.Y. Fang, S. Cheng, W.M. Sun, H.A.A. Noreldeen, Q. Zhang, H.H. Deng, W. Chen, De novo design of a photoluminescent sensor for baicalin detection via regulating molecule-like charge transfer of gold nanocluster, Sensors Actuators B Chem. 368 (2022) 132197, https://doi.org/10.1016/j.snb.2022.132197.

[51] S. Govindaraju, S.R. Ankireddy, B. Viswanath, J. Kim, K. Yun, Fluorescent gold nanoclusters for selective detection of dopamine in cerebrospinal fluid, Sci. Rep. 7 (2017) 1–12, https://doi.org/10.1038/srep40298.

[52] Á. Juhász, E. Csapó, D. Ungor, G.K. Tóth, L. Vécsei, I. Dékány, Kinetic and thermodynamic evaluation of kynurenic acid binding to GluR1270-300 polypeptide by surface plasmon resonance experiments, J. Phys. Chem. b. 120 (2016) 7844–7850, https://doi.org/10.1021/acs.jpcb.6b05682.

[53] S. Al-Omari, Separation of static and dynamic thermodynamic parameters for the interaction between pyropheophorbide methyl ester and copper, J. Porphyr. Phthalocyanines. 18 (2014) 297–304, https://doi.org/10.1142/S1088424614500023.